Materials Horizons

ROYAL SOCIETY OF CHEMISTRY

COMMUNICATION

View Article Online
View Journal | View Issue

Cite this: *Mater. Horiz.*, 2025, **12**, 5702

Received 10th March 2025,
Accepted 14th May 2025

DOI: 10.1039/d5mh00426h

rsc.li/materials-horizons

Structural amine-induced interfacial electrical double layers for efficient photocatalytic H_2 evolution†

Jing Deng,‡[ab] Xinyu Xu,‡[ab] Bo Su,[ab] Minghui Liu,*[c] Xiahui Lin,[ab] Wandong Xing,*[ab] Xue Feng Lu,[ab] Zhian Lan,[ab] Guigang Zhang[ab] and Sibo Wang*[ab]

The efficiency of photocatalytic hydrogen evolution is fundamentally constrained by limited charge carrier separation. Herein, we deliberately engineered an electric double layer (EDL) *via* surface modification with positively charged molecules, which optimizes the charge carrier dynamics. The anchoring of both diethylenetriamine (DETA) molecules and Pt species on CdS (denoted as Pt/CdS-D) achieves remarkable H_2 evolution performance, delivering an exceptional rate of 6295 μmol g^{-1} h^{-1} and an apparent quantum efficiency of 14.9%, which is 26.7-fold enhanced compared to that of CdS. The synergistic modification strategy concurrently lowers the activation energy barrier for water reduction and establishes EDL-driven directional charge transport channels that boost carrier separation efficiency. This work provides a paradigm for designing high-performance photocatalysts through the rational integration of functional organic groups and cocatalysts, opening new avenues for advanced solar-to-hydrogen energy conversion systems.

New concepts

This study demonstrates that the effect of diethylenetriamine-mediated interfacial electrical double layers can effectively separate the photoexcited carriers and reduce the free energy of water dissociation, achieving excellent photocatalytic H_2 production efficiency. The concept is aimed at finding an efficient strategy for H_2 generation, cooperating with a typical cocatalyst to improve activity and stability. We believe that this work and underlying concepts can help readers understand more about the mechanism of photocatalytic H_2 production and provide new strategies for designing advanced catalysts to improve H_2 production from water by solar energy.

Introduction

Photocatalytic water splitting for hydrogen production has been recognized as a pivotal pathway toward realizing a sustainable green hydrogen economy.[1,2] To date, numerous semiconductor materials (*e.g.*, sulfides,[3–5] oxides[6–8] and metal-free polymers[9–11]) have been used for hydrogen evolution applications. Among them, hexagonal wurtzite structure cadmium sulfide (CdS) stands out due to its optimal electronic structure, tunable structural properties, and visible-light responsiveness, demonstrating remarkable potential in photocatalytic hydrogen generation.[12] However, the practical deployment of the single-component CdS in achieving high-efficiency and durable photocatalytic hydrogen evolution still suffers from the rapid recombination of photogenerated electron–hole pairs, sluggish surface reaction kinetics, and intrinsic photocorrosion.[13,14]

To address these bottlenecks, multifaceted strategies have been developed to enhance the photocatalytic performance of CdS, including heterojunction construction,[15–17] defect engineering,[18–20] functional group modification,[21–23] cocatalyst loading,[24,25] *etc.* Notably, noble metal platinum (Pt) was widely employed as a hydrogen evolution cocatalyst due to its low overpotential and exceptional catalytic activity.[26–28] Nevertheless, the interfacial charge transfer efficiency of the Pt/CdS composite remains constrained by the insufficient surface electron accumulation, which limits their exploitation for photocatalytic hydrogen generation. Recent advances introduced the interfacial electrical double layer (EDL) effect as a novel paradigm to regulate surface charge distribution in photocatalysts.[29–32] By strategically decorating surfaces with charged molecular species, directional migration of photogenerated carriers can be engineered. Recently, Zhou *et al.*[30] demonstrated that grafting ester-functionalized CuNi alloy cocatalysts onto CdS surfaces establishes an EDL-induced polarization field, thereby optimizing carrier dynamics and surface atomic

[a] *State Key Laboratory of Chemistry for NBC Hazards Protection, College of Chemistry, Fuzhou University, Fuzhou 350116, China. E-mail: xwd@fzu.edu.cn, sibowang@fzu.edu.cn*

[b] *State Key Laboratory of Photocatalysis on Energy and Environment, College of Chemistry, Fuzhou University, Fuzhou 350116, P. R. China*

[c] *College of Chemistry and Materials, Jiangxi Normal University, Nanchang, Jiangxi 330022, China. E-mail: minghuiliu@jxnu.edu.cn*

† Electronic supplementary information (ESI) available. See DOI: https://doi.org/10.1039/d5mh00426h

‡ Contributed equally to this work.

chemical coordination, and achieving superior hydrogen evolution efficiency. However, when the most common positively charged molecular modifiers are used to functionalize the cocatalysts, the electron extraction capacity and spatial range remain suboptimal.

Herein, we propose the incorporation of amine groups as scoped surface modifiers, leveraging their positive charge density to significantly amplify photoelectron extraction efficiency. We have designed a dual-component synergistic modification strategy, synthesizing a CdS-based composite photocatalyst decorated with Pt nanoparticles and diethylenetriamine (DETA) molecules (denoted as Pt/CdS-D). The optimized Pt/CdS-D exhibits an exceptional hydrogen evolution rate of 6295 μmol g^{-1} h^{-1} and an apparent quantum efficiency (AQE) of 14.9% at 395 nm. Moreover, it manifests remarkable stability and reusability, maintaining consistent performance over six consecutive cycles without discernible deactivation. Combined characterizations *via* X-ray photoelectron spectroscopy (XPS), and femtosecond transient absorption spectroscopy (fs-TAS), together with density functional theory (DFT) calculations, reveal that the positively charged DETA molecules form an EDL structure on CdS, generating efficient carrier transport channels to drive photoelectron accumulation at the surface. Subsequently, Pt nanoparticles act as electron relays, facilitating directional electron transfer to proton reduction sites. The efficient spatial separation of excited charge carriers not only enhances the photocatalytic activity but also suppresses the surface accumulation of photogenerated holes, thereby mitigating photocorrosion-caused degradation. This "EDL modulation-cocatalysis synergy" mechanism addresses the intertwined challenges of insufficient surface charge accumulation and sluggish charge transfer kinetics in CdS photocatalysis.

Results and discussion

Fabrication and characterization of the photocatalyst

The CdS-D samples with DETA modification were synthesized *via* hydrothermal treatment using cadmium acetate and thiourea as precursors (Scheme 1). Subsequently, the CdS counterpart was obtained by thermal removal of organic functionalities from CdS-D. And Pt nanoparticles were then deposited onto their surface, denoted as Pt/CdS-D and Pt/CdS, respectively. X-ray diffraction (XRD) analysis (Fig. 1a) confirms that the wurtzite-type CdS was successfully synthesized in all samples.[33,34] The Fourier transform infrared (FTIR) spectra (Fig. 1b) reveal distinct peaks corresponding to organic functional groups in the CdS-D and Pt/CdS-D samples, which was absent in the CdS and Pt/CdS samples.[35] No additional characteristic peaks emerge in the spectra before and after Pt loading. In addition, Brunauer–Emmett–Teller measurements indicate type-II nitrogen adsorption–desorption hysteresis loops for all catalysts (Fig. 1c and Fig. S1, ESI†). Compared with the CdS and Pt/CdS, the DETA-modified CdS-D and Pt/CdS-D samples exhibit a significant increase in specific surface area and reduced pore size (Fig. S2, ESI†), exposing the effectiveness of DETA-modification in tailoring the texture properties. Furthermore, the subsequent Pt deposition process shows a negligible impact on the structural modifications.

Morphological evolution induced by DETA decoration was studied by scanning electron microscopy (SEM) and transmission electron microscopy (TEM). Both catalysts exhibit randomly stacked nanorod architectures, while notable dimensional differences are observed. The Pt/CdS-D and CdS-D nanorods display reduced diameters (5–20 nm) (Fig. 1d–f and Fig. S3, ESI†) compared to the CdS and Pt/CdS counterparts (20–30 nm) (Fig. S4 and S5, ESI†), suggesting amine-mediated growth regulation. High-resolution TEM imaging resolves distinct lattice fringes with an interplanar spacing of 0.34 nm, corresponding to the (002) plane of CdS, as shown in Fig. 1g. Energy dispersive spectrometer (EDS) elemental mappings confirm the homogeneous distribution of constituent elements and complete removal of organic residues (Fig. 1h–l). Remarkably, Pt deposition preserves the original nanostructure without inducing morphological alterations, as evidenced by identical nanorod dimensions pre- and post-loading.

X-ray photoelectron spectroscopy (XPS) analysis was conducted to probe the surface electronic states and elemental composition. As shown in Fig. S6 (ESI†), the XPS signal of CdS reveals systematic positive shifts relative to CdS-D for Cd 3d (+0.50 eV), S 2p (+0.45 eV), and N 1s (+0.45 eV) orbitals. This uniform anodic displacement signifies a reduced electron cloud density at the CdS surface compared to its CdS-D counterpart, providing direct spectroscopic evidence for the electron-withdrawing effect induced by surface-anchored amine functional groups. Compared with the CdS-D, Pt/CdS-D shows significant positive shifts in binding energies for Cd 3d (+0.35 eV), S 2p (+0.35 eV), and N 1s (+0.25 eV) orbitals (Fig. S7, ESI†), indicating that electron transfers from CdS-D to the surface Pt species. Furthermore, the Pt/CdS catalyst presents negligible

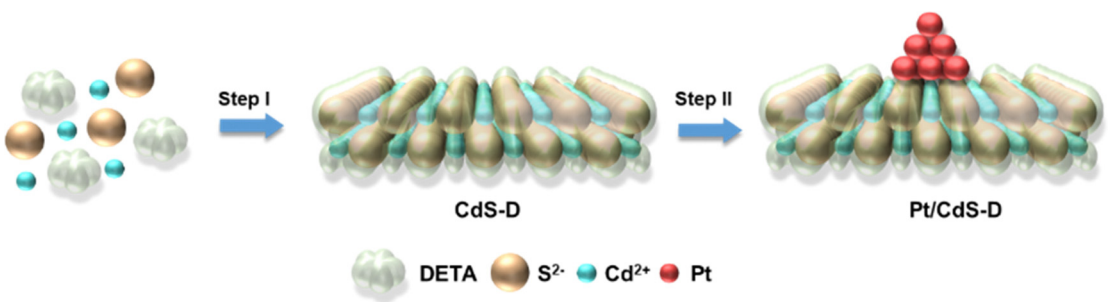

Scheme 1 Schematic illustration of the synthetic process of Pt/CdS-D.

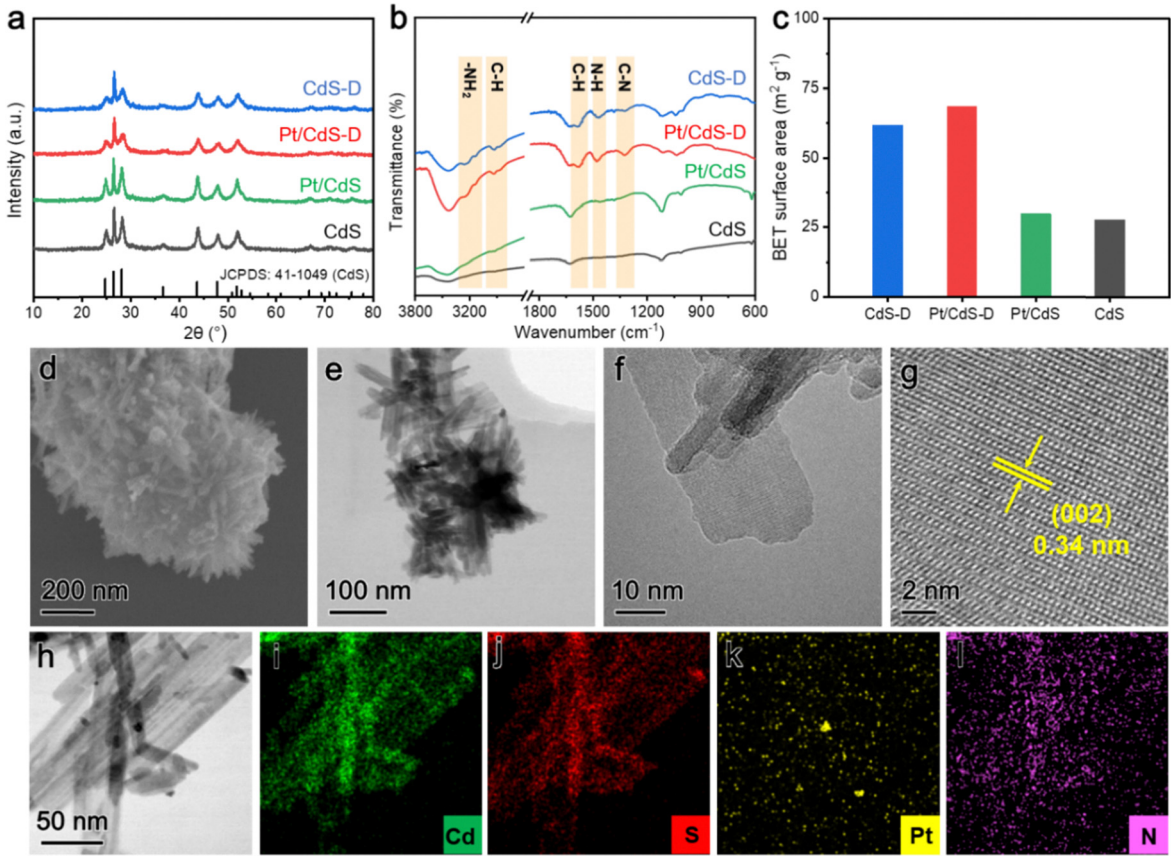

Fig. 1 (a) XRD patterns, (b) FT-IR spectra, and (c) BET surface areas of CdS-D, Pt/CdS-D, Pt/CdS and CdS. (d) SEM image, (e,f) TEM images, (g) HRTEM image, and (h)–(l) elemental mappings of Pt/CdS-D.

binding energy shifts compared to CdS (Fig. S8, ESI†), further demonstrating the critical role of organic functional groups in facilitating interfacial charge transfer dynamics. Besides, zeta potential tests reveal the positive potential of the surface of CdS-D (Fig. S9, ESI†), and this charge redistribution facilitated the directional migration of photogenerated electrons from the CdS bulk phase to the surface through strong electrostatic interactions, further confirming the above conclusion.

The diffuse reflectance spectroscopy (DRS) spectra reveal that all samples exhibit strong light absorption across the UV-visible range. The Pt/CdS-D and CdS-D samples display a slight blue-shift in their absorption edge, which is attributed to the modification by DETA molecules,[36] while loading Pt markedly enhances the light absorption capability of the catalysts (Fig. S10a, ESI†). Tauc plot extrapolation determines direct optical gap energies of 2.00 eV for Pt/CdS-D (Fig. S10b and Table S1, ESI†). Mott–Schottky tests reveal modified band alignments (Fig. S10c–f, ESI†): Pt/CdS-D exhibits a cathodically shifted conduction band (−0.72 eV *vs.* NHE) and valence band (1.28 eV). This tailored band structure would promote stronger reducing capability and keep sufficient oxidative potential for photocatalytic reactions.

Photocatalytic performance of H_2 reduction

Photocatalytic performance was evaluated under visible light irradiation (λ = 395 nm) using a Na_2S–Na_2SO_3 aqueous solution as a hole scavenger. The catalytic activity establishes a significant dependence on the DETA concentration (Fig. S11, ESI†) and Pt loading (Fig. S12, ESI†) during the synthetic process, the CdS sample displays a hydrogen evolution rate (HER) of 236 μmol g^{-1} h^{-1}. The CdS-D sample with DETA modification markedly enhances the HER to 758 μmol g^{-1} h^{-1}, while the Pt/CdS catalyst achieves a HER of 427 μmol g^{-1} h^{-1} (Fig. 2a). Remarkably, the synergistic Pt/DETA co-modified catalyst Pt/CdS-D exhibits a superior HER of 6295 μmol g^{-1} h^{-1}, accomplishing a 26.7-fold enrichment over pristine CdS, corresponding to a turnover number (TON) of *ca.* 61.12, which surpasses the most reported sulphide-based photocatalysts under comparable conditions (Fig. 2b and Table S2, ESI†).[37–50]

The AQE values of Pt/CdS-D for the photocatalytic HER under different wavelengths correspond well with the UV-Vis absorption spectra (Fig. 2c), providing evidence that the HER is driven by photoexcitation of the catalyst. Strikingly, the AQE value reaches up to 14.9% at 395 nm. In cycling tests, Pt/CdS-D retains 85% of its initial activity after six consecutive cycles with a total operation of 12 h (Fig. 2d), while Pt/CdS and CdS suffer 50% and 25% activity loss after four cycles, respectively (Fig. S13, ESI†). Post-reaction characterizations, including XRD, FTIR, SEM, HRTEM and N_2 physisorption analysis confirm structural integrity and the absence of organic degradation (Fig. S14, ESI†), underscoring the dual role of DETA in stabilizing surface Pt species and

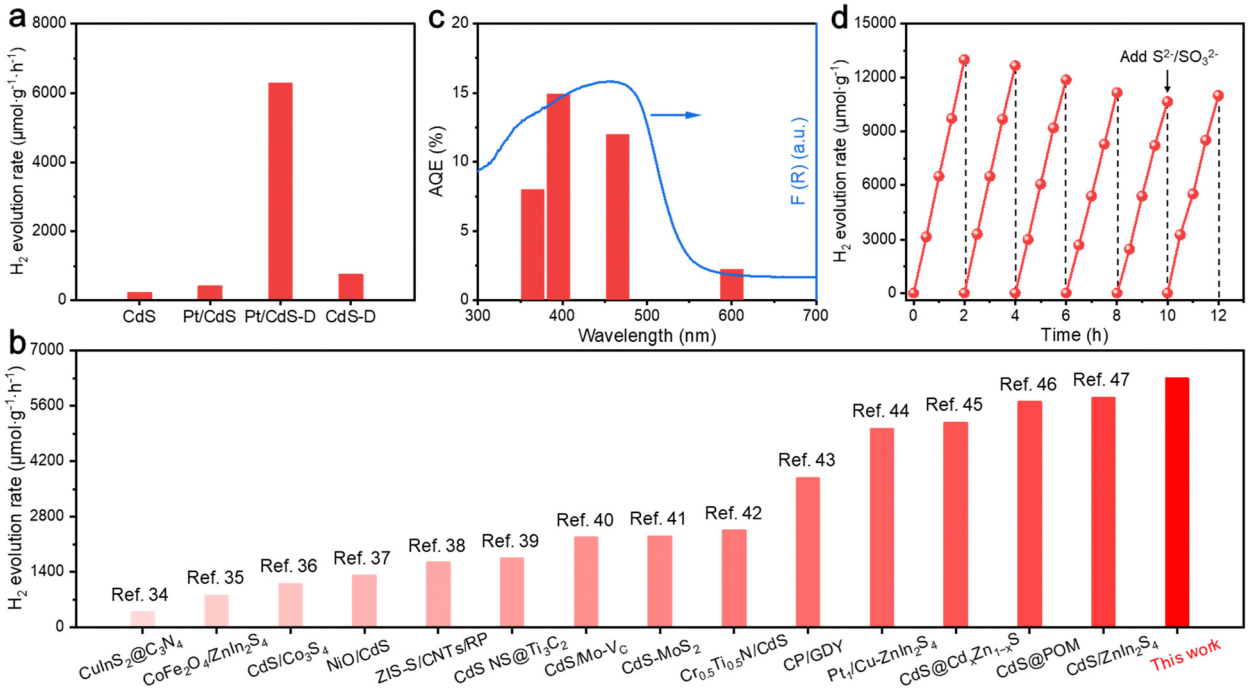

Fig. 2 (a) Photocatalytic H_2 evolution activities of CdS-D, Pt/CdS-D, Pt/CdS and CdS. (b) Comparison of the H_2 evolution rate of Pt/CdS-D with those of other typical sulfide photocatalysts under comparable conditions. (c) Wavelength-dependent AQE and DRS spectrum of Pt/CdS-D. (d) Time courses of H_2 production over Pt/CdS-D for six repeated cycles.

preventing the photocorrosion of CdS. These results validate that the synergistic interplay between organic–inorganic components enhances both catalytic activity and durability.

To reveal the universality of amine modification for activity enhancement, ethylenediamine (EDA) and triethylenetetramine (TETA) were further used to replace DETA to vary the amine group. XRD patterns and FT-IR spectra determine the successful preparation of the catalysts (Fig. S15a, b, d and e, ESI†). To our delight, the different precursors of the amine group can still greatly improve the activity of CdS (Fig. S15c and f, ESI†), demonstrating the specific role of the amine group in improving the performance of the materials.

Charge-carrier dynamics and band structure of the catalysts

For Pt/CdS-D, steady-state photoluminescence (PL) spectra reveal substantially quenched emission intensity (Fig. 3a),[11,51] and the time-resolved fluorescence spectroscopy (Fig. 3b and Table S3, ESI†) further demonstrates a longer average carrier lifetime of 9.79 ns, quantitatively confirming the synergistic role of co-modification in prolonging charge carrier separation.[52,53] Nyquist plots of Pt/CdS-D exhibit a lower charge-transfer resistance than CdS, Pt/CdS and CdS-D (Fig. 3c).[54–56] Consistently, the Pt/CdS-D electrode delivers a much higher photocurrent density than the other samples (Fig. S16, ESI†).[57,58] These collective observations establish that the Pt-DETA dual modification concurrently enhances the charge separation efficiency, interfacial kinetics, and operational durability through electronic structure modulation and surface stabilization effects.

The charge carrier kinetics in the catalysts were systematically investigated using femtosecond transient absorption spectroscopy (fs-TAS), as shown in Fig. 3d and e. Both Pt/CdS and Pt/CdS-D exhibit characteristic ground state bleaching (GSB) and excited state absorption (ESA) signatures. The emergence of a GSB peak at 500 nm within 400 fs (Fig. 3f) indicates ultrafast exciton generation in Pt/CdS-D. Subsequent intensification of the GSB signal during the initial 1400 fs period reflects hot exciton cooling to the 1Σ energy level (Fig. 3h). The concomitant emergence and growth of ESA peaks in both catalysts can be attributed to state-specific interactions between biexcitons, where the cooling of one hot exciton induces energy elevation in its counterpart. Notably, the ESA peaks exhibited progressive red-shifting due to interband interactions between the 1Σ excitonic band and adjacent energy levels. In Pt/CdS-D, the GSB signal predominantly originates from electron population in the conduction band, with negligible contribution from hole states due to their high degeneracy. The temporal evolution of the GSB peak at 500 nm primarily reflects photoelectron generation and subsequent quenching processes. As demonstrated in Fig. 3f, g and Fig. S17 (ESI†), the intensity attenuation of this peak corresponds to electron migration and recombination events. The biphasic decay profile reveals picosecond-scale electron transfer processes and nanosecond-range radiative recombination.[59,60]

Kinetic analysis (Fig. 3i and Table S4, ESI†) yields the GSB decay constants of Pt/CdS-D (379.95 ps) and Pt/CdS (18.57 ps). The prolonged decay time in Pt/CdS-D suggests the enhanced charge separation. Tri-exponential fitting reveals three characteristic lifetimes spanning picosecond to nanosecond timescales. Combined with PL data, the decay pathways of photogenerated electrons of Pd/CdS-D and Pt/CdS are summarized in Fig. 4a and

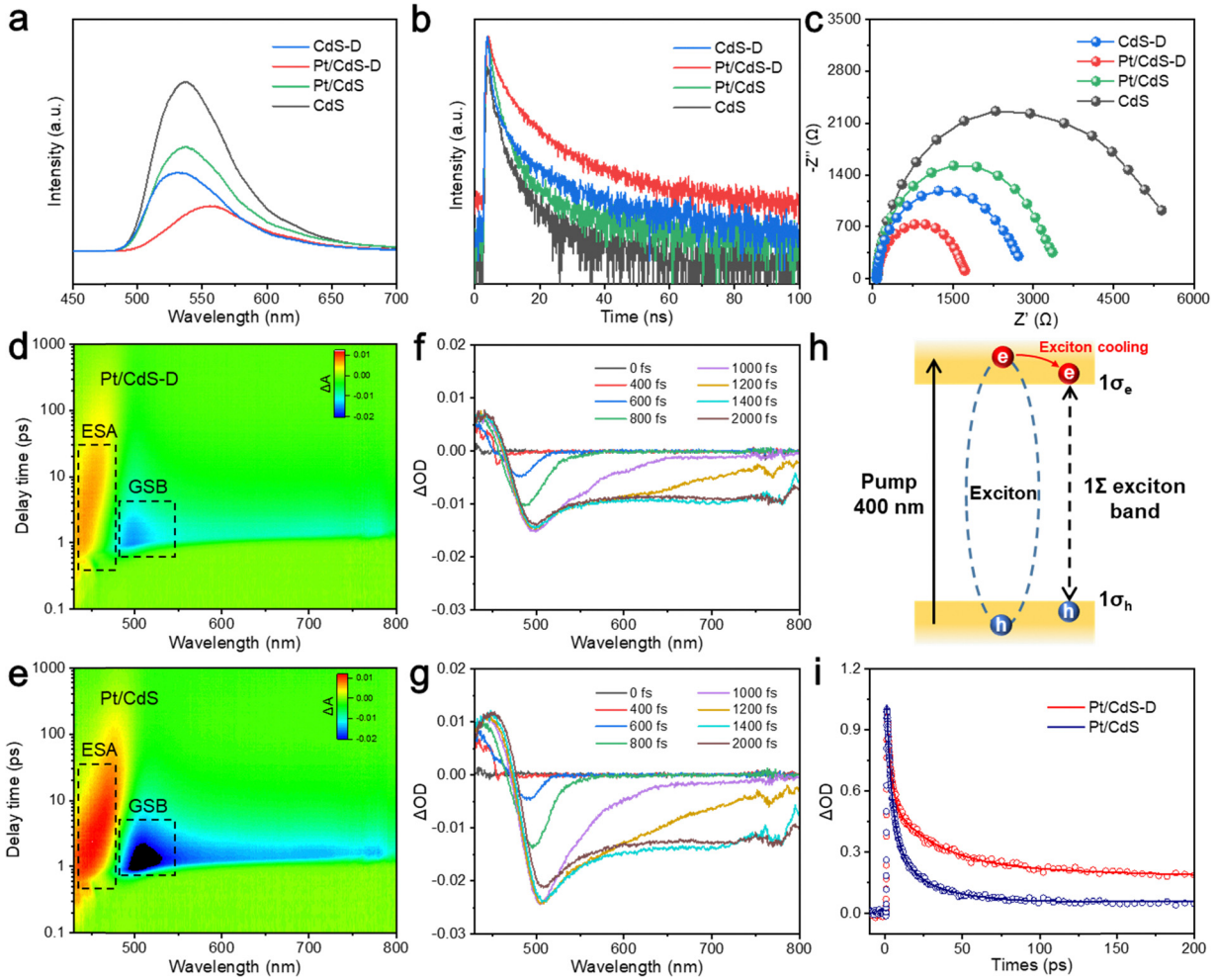

Fig. 3 (a) Steady-state PL spectra, (b) TRPL spectra and (c) EIS spectra of CdS-D, Pt/CdS-D, Pt/CdS and CdS. (d) and (e) Pseudocolor plots of (d) Pt/CdS-D and (e) Pt/CdS. (f) and (g) fs-TAS spectra of (f) Pt/CdS-D and (g) Pt/CdS within 2000 fs. (h) Schematic for the hot exciton cooling process. (i) Normalized decay kinetic curves of Pt/CdS-D and Pt/CdS at 500 nm.

Fig. S18 (ESI†), respectively. For Pt/CdS-D, three dominant electron quenching pathways are identified: (1) rapid electron trapping by metallic Pt ($\tau_1 \approx 2.7$ ps); (2) electron–hole recombination through surface-trapped holes (h-TS, $\tau_2 \approx 30.3$ ps); (3) band-edge recombination between conduction band minimum electrons and valence band maximum holes ($\tau_3 \approx 457.7$ ps). The invariant τ_1 between Pt/CdS and Pt/CdS-D indicates negligible DETA influence on primary electron trapping. The extended τ_2 reflects partial passivation of hole-trapping defects by DETA, reducing available recombination centers. The significantly prolonged τ_3 demonstrates effective suppression of radiative recombination through DETA-induced electron confinement, thereby extending the photoelectron lifetime. This coordinated charge management mechanism elucidates the superior photocatalytic performance of Pt/CdS-D.

Mechanism in the H_2 production process of the catalysts

Density functional theory (DFT) calculations revealed the charge density difference diagram (Fig. S19, ESI†) and the plane average charge density difference map of the Pt/CdS-D interface model (Fig. 4b), confirming the transfer of electrons from CdS to DETA and the formation of an electrical double layer (EDL). Therefore, the positively charged DETA species can induce a localized positive charge distribution at the interface between CdS, which is also identified by the zeta potential analysis (Fig. S9, ESI†). This charge redistribution facilitates the directional migration of excited electrons from the CdS bulk phase to the surface *via* strong electrostatic interactions. Subsequently, the deposited Pt co-catalyst further promotes electron extraction from the CdS surface. This multi-level charge transfer mechanism ultimately achieves effective spatial separation of photoinduced electron–hole pairs.

Hydrogen adsorption Gibbs free energy (ΔG_H) calculations (Fig. 4c) demonstrate optimal binding characteristics for Pt/CdS-D ($\Delta G_H = -0.26$ eV), approaching the thermoneutral ideal ($\Delta G_H = 0$ eV). This contrasts with strong adsorption for Pt/CdS (−0.55 eV) and overly weak binding for CdS-D (0.74 eV). The balanced proton adsorption/desorption dynamics on the Pt/CdS-D align with its superior photocatalytic HER performance, confirming the critical role of electronic synergy

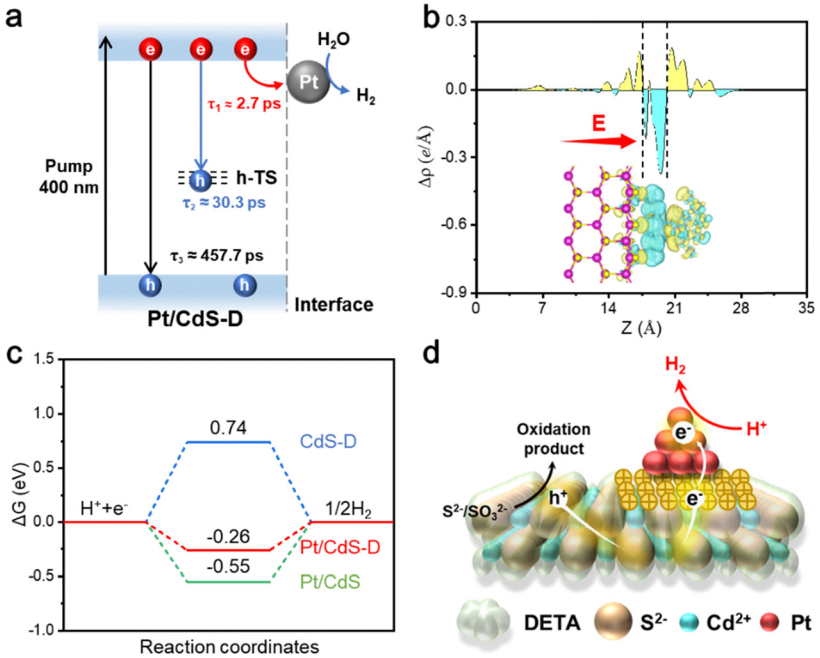

Fig. 4 (a) The schematics for electron quenching in Pt/CdS-D. (b) The 3D isosurface charge density difference in Pt/CdS-D. The cyan and yellow areas represent the electron depletion and accumulation, respectively. (c) The calculated free energy diagrams for H_2 production for CdS-D, Pt/CdS-D and Pt/CdS. (d) The possible photocatalytic mechanism of EDL-mediated charge trapping above Pt/CdS-D.

between Pt nanoparticles and amine functionalities in optimizing charge carrier separation and surface reaction kinetics. The possible photocatalytic mechanism of EDL-mediated charge trapping was proposed, as shown in Fig. 4d. Pt nanoparticles act as electron relays, facilitating directional electron transfer to proton reduction sites for efficient H_2 evolution, while photogenerated holes are scavenged by sacrificial agents. This spatially resolved separation of photogenerated charge carriers not only enhances photocatalytic activity by suppressing bulk recombination losses but also mitigates surface accumulation of oxidative species, thereby alleviating photocorrosion-induced degradation *via* oxidative etching pathways.

Conclusions

In summary, we have proposed a dual-modification tactic involving negatively charged molecular modifiers to engineer an interfacial EDL on catalyst surfaces, which effectively optimizes photoexcited carrier dynamics through spatially resolved charge separation. The Pt/CdS-D photocatalyst realizes an exceptional hydrogen evolution rate of 6295 μmol g^{-1} h^{-1} and an AQE of 14.9%. Studies combining XPS, fs-TAS, and DFT reveal that DETA coordination modulates interfacial electron transfer through ligand-to-metal charge transfer pathways, while the Pt cocatalyst provides augmented proton reduction sites. The dual-modification lowers the activation energy barrier for water reduction and the EDL-induced carrier transport channels enhance charge separation efficiency, collectively contributing to the superior photocatalytic activity and durability.

Data availability

The data supporting this article have been included as part of the ESI.†

Conflicts of interest

The authors declare no conflict of interest.

Acknowledgements

This work was financially supported by the National Natural Science Foundation of China (22432003, 22372035, 22302039, and 22311540011) and the 111 Project (D16008). The authors acknowledge Beijing PARA-TERA Tech Co., Ltd for providing access to high-performance computing resources.

Notes and references

1 S. Wang, Y. Wang, S. L. Zhang, S.-Q. Zang and X. W. Lou, *Adv. Mater.*, 2019, **31**, 1903404.
2 M. Herran, S. Juergensen, M. Kessens, D. Hoeing, A. Köppen, A. Sousa-Castillo, W. J. Parak, H. Lange, S. Reich, F. Schulz and E. Cortés, *Nat. Catal.*, 2023, **6**, 1205–1214.
3 J. Wan, Y. Wang, J. Liu, R. Song, L. Liu, Y. Li, J. Li, J. Low, F. Fu and Y. Xiong, *Adv. Mater.*, 2024, **36**, 2405060.
4 S. Wang, B. Y. Guan, X. Wang and X. W. Lou, *J. Am. Chem. Soc.*, 2018, **140**, 15145–15148.
5 B. Li, W. Wang, J. Zhao, Z. Wang, B. Su, Y. Hou, Z. Ding, W.-J. Ong and S. Wang, *J. Mater. Chem. A*, 2021, **9**, 10270–10276.

6 H. You, S. Li, Y. Fan, X. Guo, Z. Lin, R. Ding, X. Cheng, H. Zhang, T. W. B. Lo, J. Hao, Y. Zhu, H.-Y. Tam, D. Lei, C.-H. Lam and H. Huang, *Nat. Commun.*, 2022, **13**, 6144.
7 R. Li, T. Takata, B. Zhang, C. Feng, Q. Wu, C. Cui, Z. Zhang, K. Domen and Y. Li, *Angew. Chem., Int. Ed.*, 2023, **62**, e202313537.
8 J. Xiao, M. Nakabayashi, T. Hisatomi, J. J. M. Vequizo, W. Li, K. Chen, X. Tao, A. Yamakata, N. Shibata, T. Takata, Y. Inoue and K. Domen, *Nat. Commun.*, 2023, **14**, 8030.
9 Q. Wang, D. Zheng, Z. Pan, W. Xing, S. Wang, Y. Hou, M. Anpo and G. Zhang, *Adv. Funct. Mater.*, 2025, 2501889.
10 H. Zhuzhang, X. Liang, J. Li, S. Xue, Y. Lin, B. Sa, S. Wang, G. Zhang, Z. Yu and X. Wang, *Angew. Chem., Int. Ed.*, 2025, e202421861.
11 Q. Wang, G. Zhang, W. Xing, Z. Pan, D. Zheng, S. Wang, Y. Hou and X. Wang, *Angew. Chem., Int. Ed.*, 2023, **62**, e202307930.
12 Z. Zhu, J. Hu, C. Hu, Y. Lu, S. Chu, F. Chen, Y. Zhang and H. Huang, *Adv. Mater.*, 2024, **36**, 2411339.
13 B. Li, F. Wei, B. Su, Z. Guo, Z. Ding, M.-Q. Yang and S. Wang, *Mater. Today Energy*, 2022, **24**, 100943.
14 J. Cai, X. Li, B. Su, B. Guo, X. Lin, W. Xing, X. F. Lu and S. Wang, *J. Mater. Sci. Technol.*, 2025, **234**, 82–89.
15 X. Liu, D. Dai, Z. Cui, Q. Zhang, X. Gong, Z. Wang, Y. Liu, Z. Zheng, H. Cheng, Y. Dai, B. Huang and P. Wang, *ACS Catal.*, 2022, **12**, 12386–12397.
16 S. Xu, Q. Gao, Z. Hu, Y. Lu, Y. Qin and Y. Li, *ACS Catal.*, 2023, **13**, 13941–13954.
17 N. Jin, Y. Sun, W. Shi, P. Wang, Y. Nagaoka, T. Cai, R. Wu, L. Dube, H. N. Nyiera, Y. Liu, T. Mani, X. Wang, J. Zhao and O. Chen, *J. Am. Chem. Soc.*, 2023, **145**, 21886–21896.
18 Y. Zhang, W. Zhou, Y. Tang, Y. Guo, Z. Geng, L. Liu, X. Tan, H. Wang, T. Yu and J. Ye, *Appl. Catal., B*, 2022, **305**, 121055.
19 X. Luan, Z. Yu, J. Zi, F. Gao and Z. Lian, *Adv. Funct. Mater.*, 2023, **33**, 2304259.
20 K. Yang, Y. Huang, T. Wang, Y. Li, Y. Du, J. Ling, Z. Fan, C. Zhang and C. Ma, *Adv. Mater.*, 2024, **36**, 2409832.
21 Z. Zhang, M. Wang, H. Zhou and F. Wang, *J. Am. Chem. Soc.*, 2021, **143**, 6533–6541.
22 J. He, B. Han, C. Xian, Z. Hu, T. Fang and Z. Zhang, *Angew. Chem., Int. Ed.*, 2024, **63**, e202404515.
23 J. Wang, Y.-X. Feng, M. Zhang, C. Zhang, M. Li, S.-J. Li, W. Zhang and T.-B. Lu, *CCS Chem.*, 2020, **2**, 81–88.
24 H. Li, R. Li, Y. Jing, B. Liu, Q. Xu, T. Tan, G. Liu, L. Zheng and L.-Z. Wu, *ACS Catal.*, 2024, **14**, 7308–7320.
25 R. Li, H. Li, X. Zhang, B. Liu, B. Wu, B. Zhu, J. Yu, G. Liu, L. Zheng and Q. Zeng, *Adv. Funct. Mater.*, 2024, **34**, 2402797.
26 Z. Xue, X. Gao, Y. Zhang, M. Yan, J. Xu and Y. Wu, *Chem. Catal.*, 2023, **3**, 100538.
27 J. Zhang, Y. Pan, D. Feng, L. Cui, S. Zhao, J. Hu, S. Wang and Y. Qin, *Adv. Mater.*, 2023, **35**, 2300902.
28 X.-l Hao, X.-s Chu, X.-y Liu and W. Li, *J. Colloid Interface Sci.*, 2022, **621**, 160–168.
29 X. Xu, Y. Cheng, X. Zhu, J. Huang, B. Zhu, J. Meng, J. Li, G. Jing, L. Zheng, S. Yang, C. Sun, H. Li, R. Yuan and Y. Zhu, *Appl. Catal., B*, 2025, **361**, 124589.
30 C. Zhou, J. Gao, Y. Deng, M. Wang, D. Li and C. Xia, *Nat. Commun.*, 2023, **14**, 3592.
31 R. Wang, M. Gao, G. Zhao, J. Chen, Z. Guo and Y. Wang, *J. Am. Chem. Soc.*, 2025, **147**, 8205–8214.
32 S. Bera, S. Sen and D. Maiti, *J. Am. Chem. Soc.*, 2024, **146**, 25166–25175.
33 X. Li, K. Dai, C. Pan and J. Zhang, *ACS Appl. Nano Mater.*, 2020, **3**, 11517–11526.
34 Z. Li, Y. Yang, K. Dai, J. Zhang and L. Lu, *Appl. Surf. Sci.*, 2019, **469**, 505–513.
35 N. Meng, C. Liu, Y. Liu, Y. Yu and B. Zhang, *Angew. Chem., Int. Ed.*, 2019, **58**, 18908–18912.
36 J. Lv, J. Liu, J. Zhang, K. Dai, C. Liang, Z. Wang and G. Zhu, *J. Colloid Interface Sci.*, 2018, **512**, 77–85.
37 J. Luo, Z. Lin, Y. Zhao, S. Jiang and S. Song, *Chin. J. Catal.*, 2020, **41**, 122–130.
38 C. Li, H. Che, P. Huo, Y. Yan, C. Liu and H. Dong, *J. Colloid Interface Sci.*, 2021, **581**, 764–773.
39 F. Zhang, H.-Q. Zhuang, J. Song, Y.-L. Men, Y.-X. Pan and S.-H. Yu, *Appl. Catal., B*, 2018, **226**, 103–110.
40 L. Wei, D. Zeng, Z. Xie, Q. Zeng, H. Zheng, T. Fujita and Y. Wei, *Front. Chem.*, 2021, **9**, 655583.
41 L. Liu, J. Liu, W. Yang, J. Wan, F. Fu and D. Wang, *J. Colloid Interface Sci.*, 2022, **608**, 482–492.
42 X. Chen, Y. Guo, R. Bian, Y. Ji, X. Wang, X. Zhang, H. Cui and J. Tian, *J. Colloid Interface Sci.*, 2022, **613**, 644–651.
43 Y. Lei, K. H. Ng, Y. Zhu, Y. Zhang, Z. Li, S. Xu, J. Huang, J. Hu, Z. Chen, W. Cai and Y. Lai, *Chem. Eng. J.*, 2023, **452**, 139325.
44 H. Liu, P. Tan, Y. Liu, H. Zhai, W. Du, X. Liu and J. Pan, *J. Colloid Interface Sci.*, 2022, **619**, 246–256.
45 X. Meng, W. Qi, W. Kuang, S. Adimi, H. Guo, T. Thomas, S. Liu, Z. Wang and M. Yang, *J. Mater. Chem. A*, 2020, **8**, 15774–15781.
46 Z. Liu, E. Cui, X. Wang and Z. Jin, *Chem. Eng. J.*, 2024, **486**, 150060.
47 L. Su, P. Wang, J. Wang, D. Zhang, H. Wang, Y. Li, S. Zhan and J. Gong, *Adv. Funct. Mater.*, 2021, **31**, 2104343.
48 S. Kai, B. Xi, Y. Wang and S. Xiong, *Chem. – Eur. J.*, 2017, **23**, 16653–16659.
49 W.-X. Shi, Z.-Y. Liu and Z.-M. Zhang, *Inorg. Chem. Front.*, 2023, **10**, 4534–4543.
50 P. Li, M. Liu, J. Li, J. Guo, Q. Zhou, X. Zhao, S. Wang, L. Wang, J. Wang, Y. Chen, J. Zhang, Q. Shen, P. Qu and H. Sun, *J. Colloid Interface Sci.*, 2021, **604** 500–507.
51 Y.-F. Wang, M.-Y. Qi, M. Conte, Z.-R. Tang and Y.-J. Xu, *Angew. Chem., Int. Ed.*, 2024, **63**, e202407791.
52 B. Su, Y. Kong, S. Wang, S. Zuo, W. Lin, Y. Fang, Y. Hou, G. Zhang, H. Zhang and X. Wang, *J. Am. Chem. Soc.*, 2023, **145**, 27415–27423.
53 B. Su, M. Zheng, W. Lin, X. F. Lu, D. Luan, S. Wang and X. W. Lou, *Adv. Energy Mater.*, 2023, **13**, 2203290.
54 Y.-F. Wang, M.-Y. Qi, M. Conte, Z.-R. Tang and Y.-J. Xu, *Angew. Chem., Int. Ed.*, 2023, **62**, e202304306.

55 F. Liu, J. Deng, B. Su, K.-S. Peng, K. Liu, X. Lin, S.-F. Hung, X. Chen, X. F. Lu, Y. Fang, G. Zhang and S. Wang, *ACS Catal.*, 2025, **15**, 1018–1026.
56 F. Wei, W. Xue, Z. Yu, X. F. Lu, S. Wang, W. Lin and X. Wang, *Chin. Chem. Lett.*, 2024, **35**, 108313.
57 M. Zhou, H. Wang, R. Liu, Z. Liu, X. Xiao, W. Li, C. Gao, Z. Lu, Z. Jiang, W. Shi and Y. Xiong, *Angew. Chem., Int. Ed.*, 2024, **63**, e202407468.
58 W. Li, Z. Liu, B. Rhimi, M. Zhou, J. Li, K. Nie, B. Yan, Z. Jiang, W. Shi and Y. Xiong, *Angew. Chem., Int. Ed.*, 2025, e202423859.
59 C. Bie, B. Zhu, L. Wang, H. Yu, C. Jiang, T. Chen and J. Yu, *Angew. Chem., Int. Ed.*, 2022, **61**, e202212045.
60 J. Zhang, G. Yang, B. He, B. Cheng, Y. Li, G. Liang and L. Wang, *Chin. J. Catal.*, 2022, **43**, 2530–2538.